New Journal of Physics
The open-access journal for physics

Metallo-dielectric core–shell nanospheres as building blocks for optical three-dimensional isotropic negative-index metamaterials

R Paniagua-Domínguez[1], F López-Tejeira[1], R Marqués[2] and J A Sánchez-Gil[1,3]

[1] Instituto de Estructura de la Materia, Consejo Superior de Investigaciones Científicas, Serrano 121, 28006 Madrid, Spain
[2] Departamento de Electrónica y Electromagnetismo, Universidad de Sevilla, 41012 Sevilla, Spain
E-mail: j.sanchez@csic.es

New Journal of Physics **13** (2011) 123017 (15pp)
Received 18 August 2011
Published 9 December 2011
Online at http://www.njp.org/
doi:10.1088/1367-2630/13/12/123017

Abstract. Materials showing electromagnetic properties that are not attainable in naturally occurring media, so-called metamaterials, have been lately, and still are, among the most active topics in optical and materials physics and engineering. Among these properties, one of the most attractive ones is the sub-diffraction resolving capability predicted for media having an index of refraction of -1. Here, we propose a fully three-dimensional, isotropic metamaterial with strong electric and magnetic responses in the optical regime, based on spherical metallo-dielectric core–shell nanospheres. The magnetic response stems from the lowest, magnetic-dipole resonance of the dielectric shell with a high refractive index, and can be tuned to coincide with the plasmon resonance of the metal core, responsible for the electric response. Since the response does not originate from coupling between structures, no particular periodic arrangement needs to be imposed. Moreover, due to the geometry of the constituents, the metamaterial is intrinsically isotropic and polarization independent. It could be realized with current fabrication techniques with materials such as silver (core) and silicon or germanium (shell). For these particular realistic designs, the metamaterials present a negative index in the range of 1.2–1.55 μm.

[3] Author to whom any correspondence should be addressed.

© IOP Publishing Ltd and Deutsche Physikalische Gesellschaft

Contents

1. Introduction

Once the possibility of building a negative-index metamaterial (NIM) was proven in the microwave regime [1], extraordinary effort was made to obtain analogous behaviour for increasingly higher frequencies up to the visible range of the electromagnetic spectrum [2, 3]. The major obstacle found when trying to translate ideas to higher frequencies was how to achieve a strong diamagnetic response in the systems designed. Many attempts to tackle the problem were simple miniaturizations of the canonical designs employed in those first metamaterials operating in microwaves. As an example, the split-ring configurations, or slight variations, were reduced up to the nanoscale to obtain such a magnetic response. Apart from the fundamental limitations inherited from those designs, e.g. anisotropy, and the increasing complexity of the fabrication procedures, several drawbacks have been found in this process, some of them being a consequence of the different behavior of metals when excited with higher frequency waves [4]. Precisely, this different behavior also inspired some authors to search for different configurations intended to exploit the plasmonic response to obtain artificial magnetism. In many of them, artificial magnetism is due to coupling between different plasmonic structures, their drawback thus being the high losses within metallic parts [5]. In most cases, the proposed designs are restricted to operate under certain polarization and incidence conditions [6–8] or are not truly three-dimensional (3D) materials [9, 10]. Moreover, in many cases, the behavior of the proposed designs stems from coupling between the different constituents, thus making particular arrangements necessary. As a consequence, spatial dispersion effects often appear due to the propagation of waves in the lattice. Lately, some approaches based on plasmonic waveguides supporting negative-index modes have pushed the frequencies in which left-handed (LH) behavior is obtained well within the visible spectrum. However, propagation inside such materials would be limited to the propagation length of the plasmon in the waveguide, thus making the design a single-layer device, lacking true three-dimensionality [9, 10]. In addition, various attempts have been made towards NIM by exploiting magnetic resonances occurring in structures made of high-permittivity materials [11–13]. Some of them combine these structures with secondary structures providing the electrical response [14–17] or embed them in a metallic host medium [18], thus having inherent high

losses. Here we report a design that tackles many of the previously mentioned limitations, namely, a totally 3D isotropic NIM, operating at optical frequencies, whose response is due to every isolated 'meta-atom'. Therefore, no particular arrangement of them is needed. We study the possibility of using a spherical core–shell configuration to obtain with a single structure both electric and magnetic responses. The core, being metallic, is responsible for the electrical response, while the shell, made of a high-permittivity dielectric, provides the strong diamagnetic response. An extension of Mie theory is exploited to rigorously determine the scattering properties and resonances of the whole spherical core–shell configuration, which essentially determines the effective material properties [19]. Calculations for core–shell structures built up with realistic materials (Ag@Si and Ag@Ge) demonstrate the possibility of obtaining NIM operating at 1.2 μm–1.55 μm. Since both responses are attained directly from a single constituent, no particular arrangement of the inclusions is needed. In order to extract the effective parameters of the metamaterial, we will assume both a random and a simple cubic distribution. In the case of a random distribution, the Lorentz–Lorenz theory is applied, leading to simultaneously negative effective permeability and permittivity for several filling fractions. In the case of a simple cubic lattice arrangement, the finite-element method is applied to carry out numerical simulations, which fully account for interaction between the periodically arranged constituents. Effective material constants are then extracted through the standard S-parameter [20, 21] retrieval procedure, and are tested to fulfill causality and passivity, thus confirming a true double-negative index. Due to the spherical symmetry of the constituents, the metamaterial response will be essentially isotropic and polarization independent.

2. Optical properties of metallo-dielectric core–shell meta-atoms

Let us examine the scattering of a plane electromagnetic wave (wavelength λ) from a spherical core–shell particle without any approximation, which indeed can be done analytically as an extension of Mie theory, obtained first by Aden and Kerker [22]. Figure 1(a) depicts the geometry of one of the basic constituents or 'meta-atoms': a high-permittivity (ϵ) dielectric shell is considered with outer radius $R \ll \lambda$ and thickness T, ϵ_c and ϵ_0 being the dielectric constants of the core and the surrounding medium, respectively. The scattering and extinction efficiencies can be expressed in terms of the material and geometrical parameters through the scattering coefficients a_l and b_l (which represent, respectively, the different electric and magnetic multipolar contributions) as

$$Q_{\text{sca}} = \frac{2}{y^2}\sum_{l=1}^{\infty}(2l+1)(|a_l|^2+|b_l|^2), \tag{1}$$

$$Q_{\text{ext}} = \frac{2}{y^2}\sum_{l=1}^{\infty}(2l+1)\Re(a_l+b_l), \tag{2}$$

where $y = kR$. The mentioned scattering coefficients can be written in terms of the spherical Bessel functions of the first ($j_l(x)$) and the second ($y_l(x)$) class and depend on ϵ_c/ϵ_0, ϵ/ϵ_0, R_{in} and R. $\Re$ denotes the real part. Their explicit form is

$$a_l = \frac{\psi_l(y)[\psi_l'(ny) - A_l\chi_l'(ny)] - n\psi_l'(y)[\psi_l(ny) - A_l\chi_l(ny)]}{\xi_l(y)[\psi_l'(ny) - A_l\chi_l'(ny)] - n\xi_l'(y)[\psi_l(ny) - A_l\chi_l(ny)]}, \tag{3}$$

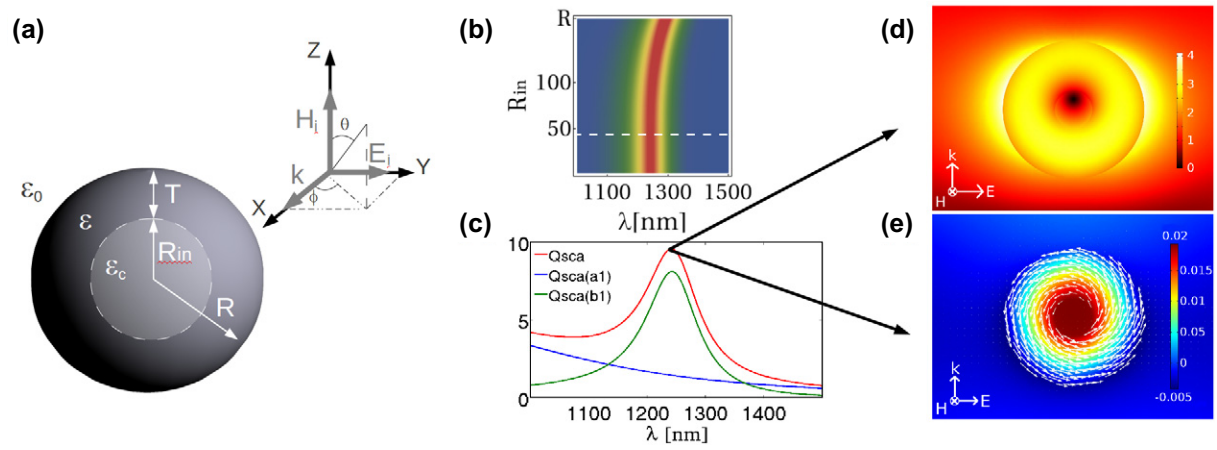

Figure 1. (a) The geometry of the problem. (b) Dipolar magnetic contribution to the total scattering efficiency of a silicon (Si) nanoshell with outer radius $R = 170$ nm as a function of the inner radius (R_{in}) and wavelength of the incident light. (c) Total scattering efficiency, together with the dipolar electric (a_1) and magnetic (b_1) contributions to the scattering efficiency for the inner radius $R_{\text{in}} = 45$ nm (indicated in (b) by a dashed white line). (d, e) Near-field plots at the magnetic resonance for the Si shell of (c). (d) Norm of electric field. (e) Out-of-plane component (only nonzero component of the incident magnetic field) of **H**, together with the electric displacement field in white arrows.

$$b_l = \frac{n\psi_l(y)[\psi_l'(ny) - B_l\chi_l'(ny)] - \psi_l'(y)[\psi_l(ny) - B_l\chi_l(ny)]}{n\xi_l(y)[\psi_l'(ny) - B_l\chi_l'(ny)] - \xi_l'(y)[\psi_l(ny) - B_l\chi_l(ny)]}. \tag{4}$$

The Ricatti–Bessel functions introduced are $\psi_l(z) = zj_l(z)$, $\chi_l(z) = -zy_l(z)$ and $\xi_l(z) = zh_l^{(1)}(z)$, where $h_l^{(1)}(z) = j_l(z) + \mathrm{i}y_l(z)$ is the spherical Hankel function of the first class. The coefficients A_l and B_l are

$$A_l = \frac{n\psi_l(nx)\psi_l'(n_cx) - m_c\psi_l'(ny)\psi_l(n_cx)}{n\chi_l(nx)\psi_l'(nx) - n_c\chi_l'(ny)\psi_l(n_cx)}, \tag{5}$$

$$B_l = \frac{n\psi_l(n_cx)\psi_l'(nx) - n_c\psi_l(ny)\psi_l'(n_cx)}{n\chi_l'(nx)\psi_l(n_cx) - n_c\psi_l'(n_cy)\chi_l(nx)}, \tag{6}$$

where $x = kR_{\text{in}}$, $n^2 = \epsilon/\epsilon_0$ and $n_c^2 = \epsilon_c/\epsilon_0$. It can immediately be realized that all information about material and geometrical properties of the core is contained in these A_l and B_l coefficients.

2.1. Magnetic resonance of a high-permittivity shell

To better understand the underlying physics, we first characterize the magnetic resonance of a nanoshell for a real dielectric material with a high refractive index. We choose silicon (Si) the refractive index of which can be considered constant, $n = \sqrt{\epsilon/\epsilon_0} \sim 3.5$, and lossless, within the near-infrared (IR) range $\lambda = 1$–$2\,\mu$m. In figure 1(b), the contribution is plotted to the total scattering efficiency of the magnetic dipolar term (b_1) as a function of R_{in} and the incidence wavelength. It is the dominant contribution, as can be seen in figure 1(c) for the specific case of $R_{\text{in}} = 45$ nm. A resonance can be clearly seen, the wavelength of which corresponds to that

of the Si compact sphere [23] when $R_{in} \to 0$ and starts to redshift when the shell thickness is thin enough ($T \lesssim R/3$) and decreases. Thus the magnetic resonance of the Si nanoshell can be tuned within a certain range of wavelengths larger than that of the Si sphere resonance.

The behavior of the electromagnetic (EM) fields at the magnetic resonance has been calculated by full-wave (finite-element method) numerical simulations [24]. The result is depicted in figures 1(d) and (e). It can be observed that the electric displacement field rotates in planes parallel to the equator, thus inducing a strong magnetic moment. This pattern clearly shows that the electrical displacement current $-i\omega\varepsilon\mathbf{E}$ is strongly confined inside the shell, and rotates along the ϕ direction around the incident H-field. Such behavior reveals that the resonance is qualitatively quite similar to the first resonance of a dielectric ring, already reported [25], following an LC model with an inductance $L \propto \mu_0 R$ associated with the circulation of the displacement current, and a capacitance $C \propto \varepsilon R$ associated with the electric energy confined in the shell. At resonance, a strong magnetic moment along the direction of the incident H-field is generated in the same qualitative way as in the dielectric ring analyzed [25].

2.2. Electric and magnetic resonances on core–shell systems

Next we analyze the mutual influence of a metallic core and a dielectric shell. With regard to the plasmon resonance of the metallic core (i.e. collective oscillations of conduction electrons), it is well known that for small spheres ($R_{in} \ll \lambda$) of dielectric permittivity $\epsilon_c(\omega)$, embedded in a medium with dielectric constant ϵ_0, the induced dipole moment is resonant at the frequency ω_{LSPR} such that $\epsilon_c(\omega_{LSPR}) = -2\epsilon_0$ [26]. Therefore, when the metallic sphere is coated with a thick dielectric layer of permittivity ϵ, the quantity driving the resonance condition is not ϵ_c itself but, instead, the ratio between the permittivities of the core and the coating. That is, for a small metal core, the resonance occurs when $\epsilon_c/\epsilon \sim -2$ is fulfilled, thus redshifting the localized surface-plasmon resonance (LSPR) with respect to that in vacuum.

The question now arises as to whether or not the shell magnetic resonance is preserved when the core is metallic. Since the confinement and rotation of the electric field inside the coating is directly related to the jump conditions for the normal component of the field between the shell and the surrounding medium [25], and since the metal is expected to avoid penetration of the field inside, no significant changes of the magnetic resonance behaviour are expected, at least for relatively small metallic cores. This will be revealed below, where we plot the scattering efficiency together with the electric and magnetic dipolar contributions. Such behaviour makes it possible to still predict the appearance of the magnetic resonance even if a metallic core is present. Furthermore, the electric and magnetic responses of a metal–dielectric core–shell nanosphere can be tuned to make both resonances coincide. Let us take silver (Ag) as the material to build up the core and Si again as a high-permittivity dielectric for the shell. Complex Ag permittivity values are taken from tabulated data [27]. Our goal is to obtain simultaneously both the resonances in the near-IR range of the electromagnetic spectrum. The LSPR will be redshifted to that wavelength such that $\epsilon_r^{Ag} \sim -2\epsilon^{Si}$. This happens at a wavelength of about 720 nm. Nevertheless, we have to keep in mind that, strictly, this would only be a good approximation for very small metallic particles with relatively thick coatings. Since we want to push the electric resonance to the IR to make it coincide with a magnetic one stemming from the Si shell, we can take increasingly larger radius for the core. When the size of a metallic particle is increased, there is a redshift in the resonance wavelength that can be explained in terms of depolarization effects [26].

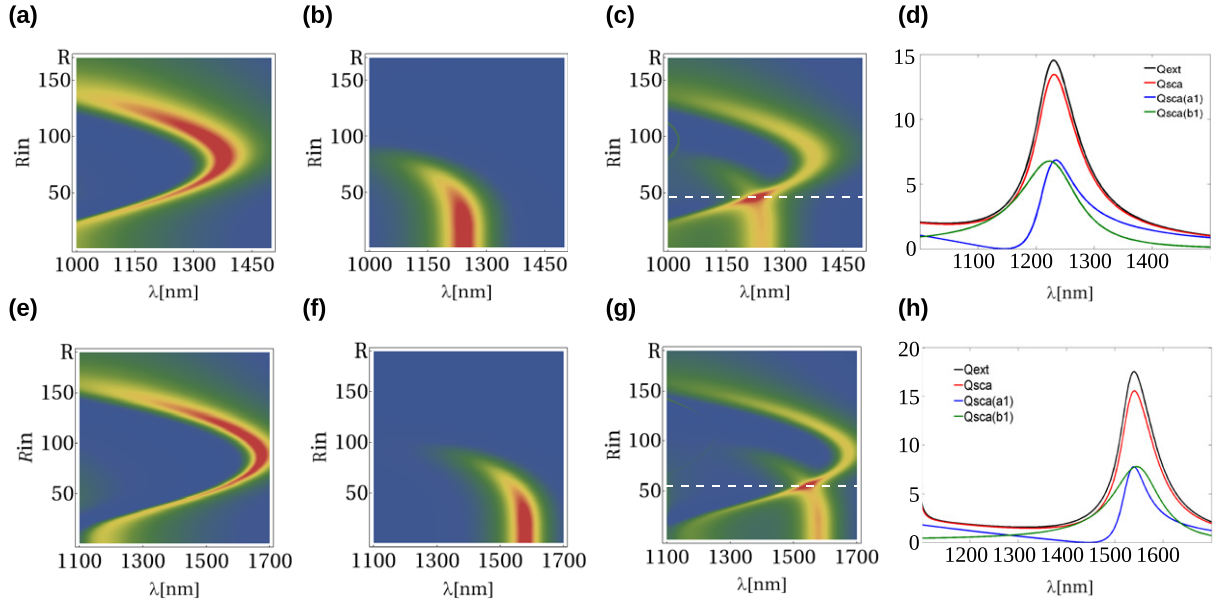

Figure 2. Optical properties of Ag@Si and Ag@Ge core–shell nanospheres. (a–c) Dipolar electric contribution (a), dipolar magnetic contribution (b) and total scattering efficiency (c) of an Ag@Si core–shell nanosphere with outer radius $R = 170\,\text{nm}$ as a function of the inner radius (R_{in}) and wavelength of the incident light. (d) Extinction and scattering efficiencies, together with the dipolar electric (a_1) and magnetic (b_1) contributions to the scattering efficiency for inner radius $R_{\text{in}} = 47\,\text{nm}$ (indicated in (c) by a dashed white line). (e–g) Dipolar electric contribution (e), dipolar magnetic contribution (f) and total scattering efficiency (g) of an Ag@Ge core–shell nanosphere with outer radius $R = 190\,\text{nm}$ as a function of the inner radius (R_{in}) and wavelength of the incident light. (h) Extinction and scattering efficiencies, together with the dipolar electric (a_1) and magnetic (b_1) contributions to the scattering efficiency for the inner radius $R_{\text{in}} = 55\,\text{nm}$ (indicated in (g) by a dashed white line).

Figures 2(a)–(c) depict both, the electric dipolar and the magnetic dipolar contributions to the scattering efficiency, together with the total scattering efficiency for an Ag@Si core–shell system of outer radius $R = 170\,\text{nm}$ as a function of R_{in} and the incidence wavelength. One can clearly see an overlap between the electric and magnetic resonances. It occurs within 1150 and 1300 nm and for inner radius $R_{\text{in}} = 40$–$50\,\text{nm}$. We have explicitly plotted the case $R_{\text{in}} = 47\,\text{nm}$ (figure 2(d)). An interesting feature that can be observed is that the magnetic resonance disappears as the inner radius increases. It can be explained by the fact that the electric displacement field in the core rotates in the opposite direction to that in the shell, thus reducing the total magnetic moment generated. Another effect can be seen in the electric dipole contribution. As the inner radius increases the resonance broadens and redshifts as expected. Interestingly, this behavior changes when the thickness is comparable with R_{in}, and the resonance starts to blueshift. This effect can be attributed to the fact that, as the dielectric shell becomes thinner, the resonance wavelength tends to that of a sphere without coating, thus blueshifting. Finally, it is important to note that the specific wavelengths at which the electric

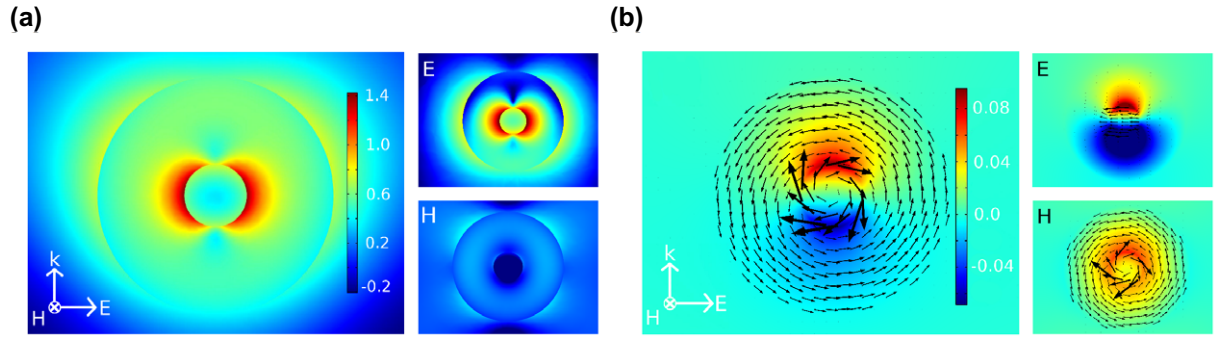

Figure 3. Near-field plots for an Ag@Si shell with $R = 170$ nm and $T = 123$ nm. (a) Norm of the electric field in $\log_{10}$ scale at combined electromagnetic resonance and when the system is excited by a purely electric excitation (top-right, E) and by a purely magnetic one (bottom-right, H). Color scale, incidence and polarization are preserved in all figures. (b) Out-of-plane component of **H**, together with the electric displacement (**D**) field in black arrows at combined electromagnetic resonance and when the system is excited by a purely electric excitation (top-right, E) or a purely magnetic one (bottom-right, H). Color scale, incidence and polarization are preserved in all figures.

and magnetic resonances overlap are determined by the geometrical parameters of the structure, as well as by the specific materials used. Therefore, it is possible to tune the wavelength of overlapping by an appropriate choice of these parameters. This gives the design a great degree of freedom, and makes it possible to operate at different frequencies. As an example, an Ag@Ge system with $R = 190$ nm is presented (figures 2(e)–(h)). In this case, resonances overlap within 1500 and 1620 nm for $R_{\text{in}} = 50$–60 nm. The particular case with $R_{\text{in}} = 55$ nm is plotted in figure 2(h).

In figure 3, the near-field pattern at the combined magnetic (shell) and electric (core) resonance is shown for the Ag@Si system. Also plotted are the responses of the system to purely electric and magnetic excitations. These were obtained by placing a perfect mirror at distances $3\lambda/4$ and λ, respectively, from the center of the structure. The distinctive behavior of both contributions is preserved in the combined electromagnetic resonance, revealed through the rotating field confined within the Si shell (as in figure 1(e)), together with the dipolar LSPR resonance of the Ag core. Note that, indeed, the electric displacements in the core and the shell rotate in opposite directions and that the magnetic near-field pattern, figure 3(b), can be explained as a combination of the electric and magnetic contributions. Near-field patterns for core–shell with Ge covers are similar to those shown here.

3. Calculation of effective parameters

What do we expect for a material consisting of such core–shell nanostructures? In general, it is highly nontrivial to extract the effective constitutive parameters of a metamaterial. Here, two different methods are applied to obtain the effective parameters of a metamaterial composed of the core–shell structures presented. In the first one, we will assume a random arrangement of the constituents, while in the second a metamaterial made of a cubic arrangement of them will be studied, both leading to negative-index behavior within certain wavelengths.

3.1. Effective parameters of a random arrangement of core–shell nanospheres

For composites made of a cubic or random arrangement of dipolar particles, the Lorentz–Lorenz theory is widely used [11, 28], leading to the well-known Clausius–Mossotti formulae relating the effective permittivity and permeability to the polarizabilities of the particles and the filling fraction $f = (4/3)\pi N R^3$, where N is the number of particles per unit volume:

$$\frac{\epsilon_{\text{eff}} - \epsilon_0}{\epsilon_{\text{eff}} + 2\epsilon_0} = f\frac{\alpha_E}{4\pi R^3}, \quad \frac{\mu_{\text{eff}} - \mu_0}{\mu_{\text{eff}} + 2\mu_0} = f\frac{\alpha_M}{4\pi R^3}, \tag{7}$$

where α_E and α_M are the electric and magnetic polarizabilities of the spherical particles. For the core–shell structures considered $R/\lambda \sim 1/7$. Therefore, we expect them to be well within the approximation considered in the theory, thus behaving essentially as electric and magnetic point dipoles. The electric and magnetic polarizabilities, α_E and α_M, respectively, are directly proportional to the scattering coefficients a_1 and b_1 (factor $\mathrm{i}(k^3/6\pi)^{-1}$). In figures 4(a) and (b), we have plotted the polarizabilities for a core–shell configuration of $R_{\text{in}} = 47$ nm and $R = 170$ nm. It is clear from the graph that there is a spectral region where negative electric and magnetic polarizabilities are obtained. Interestingly, as mentioned before, no particular arrangement of the constituents is necessary to build the metamaterial, since the resonant electric and magnetic responses arise from each core–shell structure separately. Thus, assuming a random distribution we can compute the effective parameters from (7) for different filling fractions. Figures 4(c)–(e) depict the calculated effective permittivity, permeability and refractive index for metamaterials made up of these Ag@Si core–shells with filling fractions $f = 1/3$, $f = 0.5$ and $f = 2/3$. The metamaterial has simultaneously negative permittivity and permeability for filling fractions higher than $f = 1/3$. For a filling fraction of $f = 2/3$, the system, moreover, has $|n_{\text{eff}}| \sim 1$, although this relatively high filling fraction would be in the limit of validity of Clausius–Mossotti formulae. In order to quantify the losses of the system, one can compute the so-called figure of merit, defined as f.o.m. $= |\Re(n_{\text{eff}})|/\Im(n_{\text{neff}})$. The computed f.o.m. in the LH spectral region for this filling fraction is indicated by the black curve, reaching a maximum value of f.o.m. ~ 0.71, corresponding to $\Re(n_{\text{eff}}) \sim -0.8$. If Ge is used instead of Si, the NIM behavior starts with lower filling fractions, due to stronger electric and magnetic responses (see figure 5 and compare the polarizabilities with those of figure 4). Superlensing capabilities are predicted for filling fractions lower than $f = 0.5$ (figures 5(c)–(e)). Again, the f.o.m. for the highest filling fraction is plotted as a black curve. In this case, it reaches a maximum value of f.o.m. ~ 0.75, corresponding to $\Re(n_{\text{eff}}) \sim -0.5$. Although far from being the best f.o.m. values reported for double-fishnet metamaterials (f.o.m. ~ 3) [7, 29], the predicted values are reasonably good, with the obvious advantage of isotropy of this proposal.

3.2. Effective parameters of a cubic periodic arrangement of core–shell nanospheres

To further test the metamaterial design, we consider now core–shell nanospheres arranged periodically at the vertices of a cubic lattice. We take germanium as the high-permittivity coating and choose the geometrical parameters as $R = 190$ nm and $R_{\text{in}} = 55$ nm. We consider the case when the cubic lattice has a period $d = 385$ nm (corresponding to a filling fraction $f \sim 0.5$). Full numerical simulations (see section 5) of propagation across infinite slabs of different thicknesses ranging from 9 to 13 unit cells are carried out to ensure convergence. Bloch boundary conditions are applied in the interfaces with adjacent cells. Therefore, coupling between structures (with an

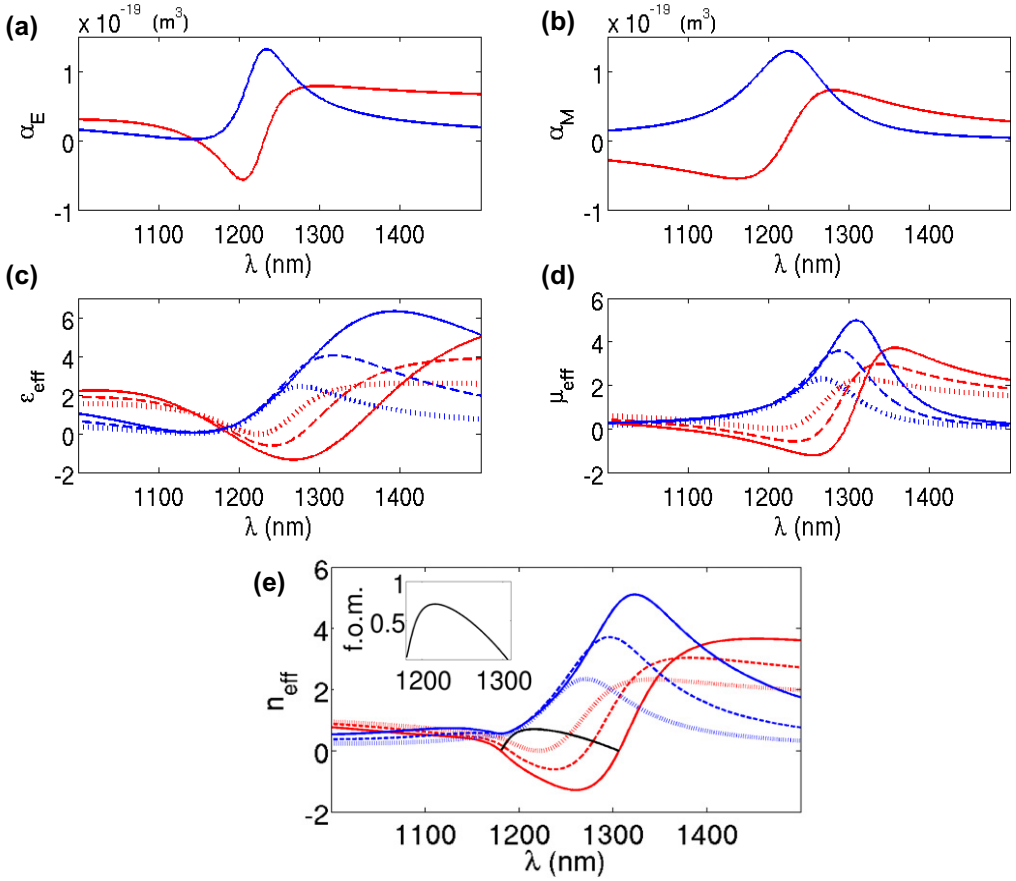

Figure 4. (a–e) Electric and magnetic polarizabilities for an Ag@Si core–shell with $R_{in} = 47$ nm and $R = 170$ nm and effective parameters for a metamaterial composed of a random arrangement of these structures. (a) Real (red) and imaginary (blue) parts of the electric polarizability. (b) Real (red) and imaginary (blue) parts of the magnetic polarizability. (c–e) Real (red) and imaginary (blue) parts of the effective permittivity (c), permeability (d) and refractive index (e) of a metamaterial with several filling fractions: $f = 1/3$ (dotted), $f = 0.5$ (dashed) and $f = 2/3$ (continuous). The black curve and the inset in (e) represent the f.o.m. for the highest filling fraction in the LH spectral region.

interparticle distance of only 5 nm) is fully considered. The spectral range of the simulation is 1.28–1.7 μm and the wave impinges at normal incidence. The effective material parameters are retrieved from the complex reflection and transmission coefficients through the usual equations found in the literature [20, 21]. While the imaginary part is unambiguously computed from the simulation, once a sufficiently high number of unit cells in the propagation direction has been considered, the real part of the index of refraction must be determined with much more care. Concretely, one must pay special attention to ensure that the retrieved refractive index fulfills causality and passivity. In this way we have obtained two bounding values for the real part of the index, so it fulfills the two mentioned requirements. For a detailed description of how the index was obtained, see section 5. In figure 6, the obtained bounds for the refractive

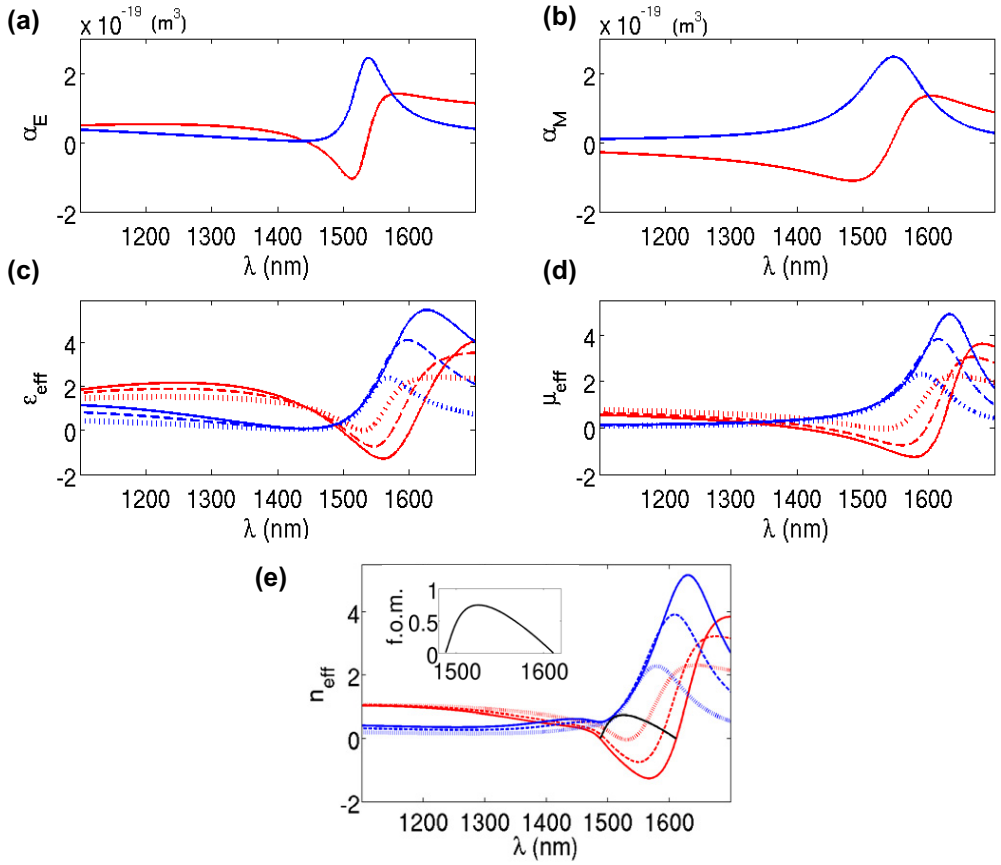

Figure 5. (a–e) Electric and magnetic polarizabilities for an Ag@Ge core–shell with $R_{\text{in}} = 55$ nm and $R = 190$ nm and effective parameters for a metamaterial composed of a random arrangement of these structures. (a) Real (red) and imaginary (blue) parts of the electric polarizability. (b) Real (red) and imaginary (blue) parts of the magnetic polarizability. (c–e) Real (red) and imaginary (blue) parts of the effective permittivity (c), permeability (d) and refractive index (e) of a metamaterial with several filling fractions: $f = 0.25$ (dotted), $f = 0.4$ (dashed) and $f = 0.5$ (continuous). The black curve and the inset in (e) represent the f.o.m. for the highest filling fraction in the LH spectral region.

index are plotted. With this retrieval technique, a negative index spectral region is predicted. In the more conservative prediction, corresponding to the higher bound, the real part of the index reaches a minimum value of $n_{\text{eff}} \sim -0.77$, with an f.o.m. ~ 1.88, corresponding to a wavelength of 1.347 μm. Although the values for the index are lower than those predicted by Clausius–Mossotti, the negative index frequency band is present and confirms the core–shell design as a meta-atom candidate for building an NIM. It needs to be pointed out that we are far from the limit of filling fractions that can be obtained with non-overlapping spheres (cannonball pile). Since, for interparticle distances as low as 5 nm, we found that coupling does not prevent the appearance of the magnetic resonance, we expect to reach higher negative values of the index in other periodic configurations with higher filling fractions. Further investigation of periodic configurations with other homogenization approaches is left for future work.

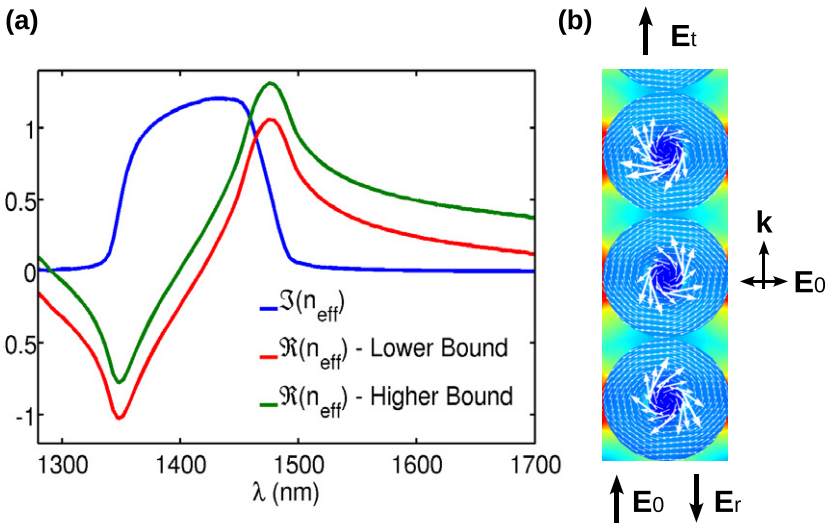

Figure 6. (a) Real and imaginary parts of the retrieved effective index of refraction of a metamaterial made by Ag@Ge core–shell nanospheres of $R = 190\,\text{nm}$ and $R_{\text{in}} = 55\,\text{nm}$ arranged at the vertices of a cubic lattice with period $d = 385\,\text{nm}$, corresponding to a filling fraction $f \sim 0.5$. (b) Detail of the normalized near electric field norm (color scale, red$\rightarrow$1, blue$\rightarrow$0) and electric displacement field (indicated by white arrows) in the periodic structure.

4. Concluding remarks and fabrication possibilities

To obtain a 3D isotropic metamaterial having negative index of refraction in the optical range of the spectrum has been one of the major challenges in the last decade for scientists and engineers devoted to electromagnetism. Here we have presented a new design based on core–shell nanospheres that operates in the near-IR, which helps tackle many of the previously found problems, namely isotropy, polarization independence and the lack of three dimensionality. In our system, the effective response of the metamaterial is due to every isolated 'meta-atom'. Therefore, no particular arrangement of the constituents is needed. Specifically, we demonstrated with realistic materials that, for a random arrangement, the system achieves double-negative index of refraction for different filling fractions and that super-resolution is possible. We also tested the validity when a very simple periodic realization is assumed. Although the achieved values in the latter case are worse than predicted by Clausius–Mossotti for the same filling fractions, we have not explored here some other periodic configurations that are expected to give a stronger response.

With regard to building these metamaterials, current silicon fabrication techniques allow the realization of complex nanostructures such as hollow nanospheres [30] and opals [31]. In some of the processes, the starting point is silica (SiO_2) nanostructures, as is the case in [31] in which Si opals are fabricated by magnesiothermic reduction of SiO_2 opals. Since silver nanospheres have been successfully covered with SiO_2 at variable thicknesses [32], there are plausible ways to realize the metamaterial proposed here, at least with Si covers. Concerning the fabrication of Ge shells instead, a layer of a different material, suitable to grow it, can be added between the core and the shell. This layer, if thin, would not affect excessively the

physical response of the system, opening the possibility of fabrication of this system as well. The underlying physical principles can, of course, be exploited at lower (far-IR and terahertz) frequencies, at which some dielectric materials exhibit very large refractive indices and certain materials (e.g. polar crystals and doped semiconductors) behave as plasmonic metals. Therefore, the results presented pave the way towards potential isotropic 3D optical metamaterials designed on the basis of the physics underlying the doubly resonant metallo-dielectric configuration.

5. Methods

Extinction and scattering cross sections based on the extended Mie theory were calculated with Wolfram Mathematica 8. The near-field plots in figures 1 and 3 were calculated using the radiofrequency (RF) module of COMSOL Multiphysics v4.0a. The computational domain consisted of four concentric spheres, which defined four subdomains. The radii of the spheres were R_{in}, R, $2R$ and $2.5R$. From the inner to the outer, the subdomains represented the core, the shell and the embedding medium (air). The last domain was set to a spherical perfectly matched layer (PML), which absorbed all scattered radiation. The incident radiation was defined as a plane wave. The mesh was constructed with the software's built-in algorithm, which generates a free mesh consisting of tetrahedral elements. The maximum element edge size was set to 15 nm in the whole core–shell structure, with a growth rate of 1.35, meaning that elements adjacent to a given one should not be bigger than 1.35 times the size of it. For the PML and air domains, the maximum element edge size was 50 nm. All mesh sizes are below the value recommended in the program specifications, which sets a maximum edge size of $1/10$ of the effective wavelength for correct meshing. Finally, for the simulation of wave propagation along an N-unit-cell-thick slab, COMSOL was also used. In this case, the computational domain consisted of two concentric spheres representing the core–shells and a right rectangular prism of width and height $d = 385$ nm and length $L = Nd$. Bloch periodic boundary conditions were set in the directions perpendicular to the propagation and two ports activated in the direction of propagation that allow us to compute the reflection and transmission complex coefficients. In these cases, the maximum element edge size was set to 40 nm in the core–shell subdomains, 50 nm in the port boundaries and 100 nm in the boundaries where periodic boundary conditions were applied. A correct solution of the problem requires identical meshing for the pairs of boundaries where periodic boundary conditions are applied. In all cases the PARDISO solver was used. As an example, for 9-unit-cell slab simulation, the total mesh consisted of 149 064 elements, and the calculation involved 948 768 degrees of freedom, requiring almost 18 GB of memory.

5.1. Effective index retrieval procedure

The effective refractive index for the metamaterial structure, shown in figure 6, was calculated from complex transmission and reflection coefficients following [21]. As mentioned before, we performed simulations of wave propagation across infinite slabs of different thicknesses. After a sufficient number of unit cells is considered, we get convergence of the results. We needed to consider up to 9 unit cells in the direction of propagation to get convergence. Then, we performed the simulation for 11- and 13-unit-cell-thick slabs.

It is well known that, when extracting the effective index through transmission and reflection coefficients, an ambiguity arises related to the branches of the complex logarithm

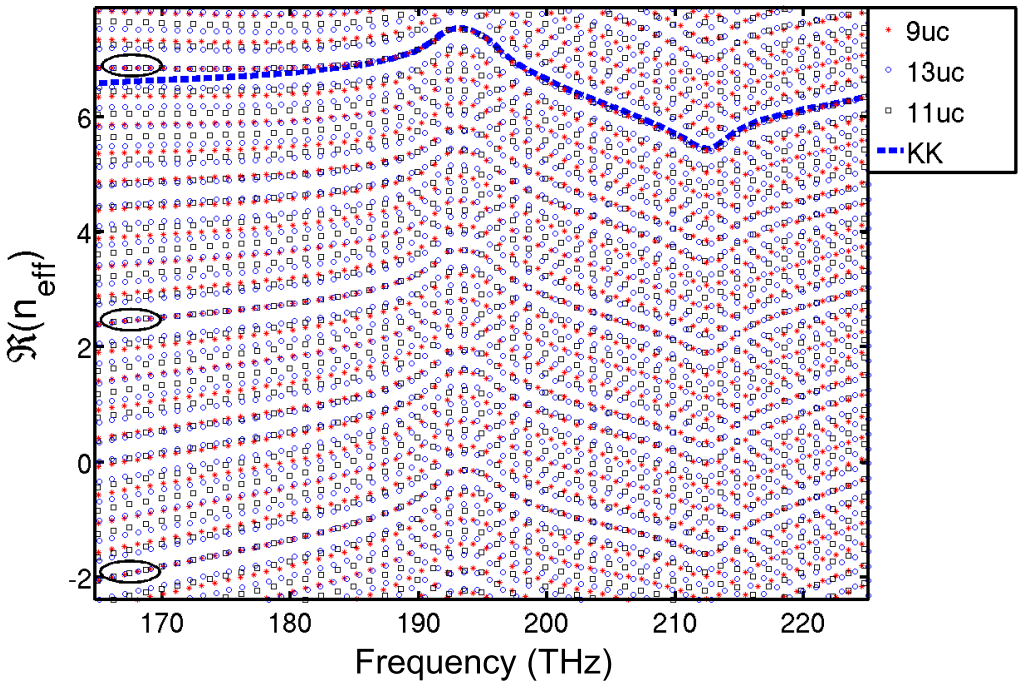

Figure 7. A very large number of branches of the real part of the retrieved refractive index for 9 (red asterisks), 11 (black squares) and 13 (blue circles) unit cells thick metamaterial slabs, composed of Ag@Ge core–shell nanospheres of $R = 190$ nm and $R_{in} = 55$ nm arranged in the vertices of a cubic lattice with period $d = 385$ nm, corresponding to a filling fraction $f \sim 0.5$. The branches that are independent of the thickness of the slab are indicated by a surrounding ellipse. The dashed blue line represents the real part obtained from the imaginary part by the Kramers–Kronig relations, plus a constant factor to fit the only thickness-independent index showing good agreement.

function. This ambiguity only affects the determination of the real part of the index, the imaginary one being univocally defined. It is a common assumption that the real part of the index can be found plotting different branches for different thicknesses. The physical index is assumed to be the one independent of the thickness of the slab. However, this assumption may be ambiguous as well. The reason is that, if one plots a sufficiently high number of branches one will find more than one unique index independent of the thickness. In figure 7, this situation is shown. We have plotted a very large number of branches corresponding to the Ag@Ge core–shell periodic configuration of section 3.2. It can be clearly seen that there is more than one situation in which the index is independent of the thickness. Therefore, although this requirement for thickness independence of the retrieved index is clearly physically acceptable, we should not take it as a sufficient condition.

In fact, we should impose more conditions on the retrieved index. It must, no doubt, fulfill the basic requirement of causality, expressed mathematically by the Kramers–Kronig relations. Since, fortunately, we can unambiguously determine the imaginary part of the index, it is possible to apply the Kramers–Kronig relations to get the real part of the index [33]. We need to point out that, actually, by this technique one can only compute the corresponding real part

up to a constant factor. The value of this factor, interpreted physically as the value of the index when the frequency tends to infinity, needs to be determined somehow. The question then, is whether any of the indices that do not depend on thickness also fulfills causality. In figure 7, the real part of the index, retrieved through the Kramers–Kronig relations applied to the imaginary part, is plotted on top of the only thickness-independent index for which the fitting is in good agreement (the constant factor added is 6.35). It is apparent that the agreement is quite good. It should be noted that this index is the only one for which the fitting is good, thus fulfilling the causality constraint.

However, one more constraint must be imposed in order to get an acceptable effective index. The resulting effective medium should be passive. This condition demands no spontaneous generation of energy and mathematically relates the real and imaginary parts of the effective index to the real and imaginary parts of the effective impedance of the slab. This impedance can be computed also from the complex reflection and transmission coefficients [21]. Applying this condition we find that none of the indices retrieved directly from the transmission and reflection complex coefficients fulfill both causality and passivity. Nevertheless, one can still compute a physically acceptable effective index of refraction. If one uses the passivity condition, it is possible to impose upper and lower bounds on the constant factor in the Kramers–Kronig relations. An index with a real part given directly by the Kramers–Kronig relations, applied to the univocally computed imaginary part, and a constant factor between the two bounds will necessarily fulfill both conditions. We found that, in fact, the upper and lower bounds imposed by passivity are quite close in value, being a restrictive condition on the possible values of the index of refraction. The two boundary values for the index are plotted in figure 6(a).

Acknowledgments

The authors acknowledge support from the Spain Ministerio de Ciencia e Innovación through the Consolider-Ingenio project EMET (CSD2008-00066) and NANOPLAS (FIS2009-11264) and from the Comunidad de Madrid (grant MICROSERES P2009/TIC-1476). RP-D acknowledges support from CSIC through a JAE-Pre grant. We are indebted to an anonymous referee for helpful suggestions on the convergence of the COMSOL results in figure 6.

References

[1] Smith D R, Padilla W J, Vier D C, Nemat-Nasser S C and Schultz S 2000 *Phys. Rev. Lett.* **84** 4184–7
[2] Shalaev V M 2007 *Nature Photonics* **1** 41–8
[3] Soukoulis C M and Wegener M 2011 *Nature Photonics* **5** 523–30
[4] Zhou J, Koschny Th, Kafesaki M, Economou E N, Pendry J B and Soukoulis C M 2005 *Phys. Rev. Lett.* **95** 223902
[5] Alú A, Salandrino A and Engheta N 2006 *Opt. Express* **14** 1557
[6] Güney D Ö, Koschny T and Soukoulis C M 2011 *Phys. Rev.* B **83** 045107
[7] Dolling G, Wegener M, Soukoulis C M and Linden S 2007 *Opt. Lett.* **32** 53–5
[8] Dionne J A, Verhagen E, Polman A and Atwater H A 2008 *Opt. Express* **16** 19001–17
[9] Burgos S P, de Waele R, Polman A and Atwater H A 2010 *Nat. Mater.* **9** 407–12
[10] Lezec H J, Dionne J A and Atwater H A 2007 *Science* **316** 430–2
[11] Wheeler M S, Aitchison J S and Mojahedi M 2005 *Phys. Rev.* B **72** 193103
[12] Zhao Q, Kang L, Du B, Zhao H, Xie Q, Huang X, Li B, Zhou J and Li L 2008 *Phys. Rev. Lett.* **101** 027402
[13] Vynck K, Felbacq D, Centeno E, Cabuz A I, Cassagne D and Guizal B 2009 *Phys. Rev. Lett.* **102** 133901

[14] Yannopapas V and Moroz A 2005 *J. Phys.: Condens. Matter* **17** 3717–34
[15] Yannopapas V and Vitanov N V 2006 *Phys. Rev.* B **74** 193304
[16] Yannopapas V 2007 *Phys. Rev.* B **75** 035112
[17] Kussow A-G, Akyurtlu A and Angkawisittpan N 2008 *Phys. Status Solidi* b **245** 992
[18] Seo B-J, Ueda T, Itoh T and Fetterman H 2006 *Appl. Phys. Lett.* **88** 161122
[19] Rockstuhl C, Menzel C, Mühlig S, Petschulat J, Helgert C, Etrich C, Chipouline A, Pertsch T and Lederer F 2011 *Phys. Rev.* B **83** 245119
[20] Smith D R, Vier D C, Koschny T and Soukoulis C M 2005 *Phys. Rev.* E **71** 036617
[21] Chen X, Grzegorczyk T M, Wu B, Pacheco J Jr and Kong J A 2004 *Phys. Rev.* E **70** 016608
[22] Aden A L and Kerker M J 1951 *Appl. Phys.* **22** 1242
[23] García-Etxarri A, Gómez-Medina R, Froufe-Pérez L S, López C, Chantada L, Scheffold F, Aizpurua J, Nieto-Vesperinas M and Sáenz J J 2011 *Opt. Express* **19** 4815
[24] COMSOL Multiphysics v4.0a
[25] Jelinek L and Marqués R 2010 *J. Phys.: Condens. Matter* **22** 025902
[26] Bohren C F and Huffman D R 1983 *Absorption and Scattering of Light by Small Particles* (New York: Wiley-Interscience)
[27] Johnson P B and Christy R W 1972 *Phys. Rev.* B **6** 4370
[28] Wheeler M S, Aitchison J S, Chen J I L, Ozin G A and Mojahedi M 2009 *Phys. Rev.* B **79** 073103
[29] Garcia-Meca C, Hurtado J, Martí J, Martínez A, Dickson W and Zayats A V 2011 *Phys. Rev. Lett.* **106** 067402
[30] Yao Y, McDowell M T, Ryu I, Wu H, Liu N, Hu L, Nix W D and Yi Cu 2011 *Nano Lett.* **11** 2949–54
[31] Ibisate M, Golmayo D and López C 2009 *Adv. Mater.* **21** 2899
[32] Aslan K, Wu M, Lakowicz J R and Geddes C D 2007 *J. Am. Chem. Soc.* **129** 1524–5
[33] Ohta K and Ishida H 1988 *Appl. Spectrosc.* **42** 952–7